

Does sink efficiency unequivocally characterize how grain boundaries impact radiation damage?

O. El-Atwani,^{1,*} E. Martinez,¹ E. Esquivel,¹ M. Efe,² C. Taylor,³ Y. Q. Wang,¹ B. P. Uberuaga,¹ and S. A. Maloy¹

¹*Materials Science and Technology Division, Los Alamos National Laboratory, Los Alamos, New Mexico 87545, USA*

²*Metallurgical and Materials Engineering, Middle East Technical University, Ankara 06800, Turkey*

³*Fusion Safety Program, Idaho National Laboratory, Idaho Falls, Idaho 83415, USA*



(Received 27 July 2018; published 21 November 2018)

The role of grain boundaries in limiting irradiation damage in nanocrystalline materials is often correlated with the grain boundary sink efficiency. Here, we demonstrate on a tungsten material system (which has very distinct vacancy and interstitial mobilities) that sink efficiency does not unequivocally describe how grain boundaries impact irradiation damage. Rather, it reflects a particular defect diffusion equation that can change if any of the bulk conditions change. Even when denuded zone formation does not occur and grain boundaries have zero sink efficiencies, grain boundaries still impact the performance of nanocrystalline materials under irradiation by acting as a saturable defect storage site. However, denuded zone formation can occur under a necessary requirement of extra defect recombination at the grain boundaries (which, for example, is not possible when vacancy migration does not occur). These insights provide answers to several outstanding questions regarding the sink efficiency of a grain boundary and assist in parametrizing the role of grain boundaries in limiting irradiation damage in nanocrystalline materials.

DOI: [10.1103/PhysRevMaterials.2.113604](https://doi.org/10.1103/PhysRevMaterials.2.113604)

I. INTRODUCTION

Materials utilized in extreme irradiation environments are exposed to far-from-equilibrium conditions that create challenges in material design, synthesis, and testing [1–3]. Evaluating the performance of existing materials and designing new irradiation-resistant materials (through manipulating existing materials or synthesizing new ones) requires understanding the fundamental atomistic processes that give rise to their irradiation tolerance under extreme irradiation conditions. Irradiation-induced defects (surviving interstitials and vacancies and their aggregates) are the origin for the atomistic changes (formation of voids, loops, bubbles, etc.) [4,5] which can alter the morphology [6–8] and compromise the mechanical properties [9–11] of irradiated materials.

Utilization of ultrafine (UF) (grain size of 100–500 nm) and nanocrystalline (NC) (grain size <100 nm) materials is one of the proposed routes for radiation-tolerant materials due to their high defect sink density (high grain boundary density). In addition to the role of the grain boundaries in enhancing the mechanical properties of UF and NC materials [12–15], grain boundaries have been shown to act as sinks for both transmutation products (e.g., He) and defects (e.g., interstitials, vacancies, and clusters of such) and enhance the propensity for defect annihilation in irradiated materials [4,16–35]. Absorption of defects by grain boundaries decreases the defect densities in the grain matrices [24–26,36,37] and, therefore, a delay (increase in the associated ion dose) in radiation-induced microstructural alterations is expected [38]. To investigate whether such improvements are adequate for the extreme

environments anticipated in advanced nuclear power systems, quantification of the performance of UF and NC materials as a function of irradiation conditions is a critical step.

Experimental studies comparing irradiation in NC materials and their coarse grain counterparts were performed previously on a few materials [24,25,39] but a clear understanding of the improvement in irradiation resistance of NC materials is still lacking. Other studies measuring defect densities in grain matrices as a function of grain size in the NC and UF regimes were also performed [26,36,37,40]. However, in some cases, a few phenomena were observed which made the quantification of the performance of UF and NC materials more complex. In some cases, a decrease in defect density was observed as the grain size increased, which was unexpected [17,25]. A recent work by El-Atwani *et al.* on ion beam irradiated UF and NC iron showed defect coalescence in the UF grains [40]. Defect coalescence can lead to lower defect densities but larger defect area, possibly leading to more integrated damage in the grain matrices. In the grain-size regime bordering between UF and NC (grains over 100 nm in diameter) of a sample where nanocrystalline and ultrafine grains coexist, scatter in the data was observed. The difference in performance of different grains was attributed to different sink efficiencies of different boundaries. Grain boundary sink efficiency (ratio of defects absorbed by a particular boundary to defects absorbed by a perfect boundary in which defects are never reemitted) [41] is a parameter that characterizes the ability of grain boundaries to absorb nearby defects and is a function of the macroscopic (manifested by the grain boundary misorientation angle and the grain boundary plane) and the microscopic degrees of freedom of a grain boundary [35]. Several studies have confirmed the effect of the grain boundary character on defect absorption in irradiated nanocrystalline materials [16,17,42].

*oelatwan25@gmail.com

Therefore, the grain boundary character must be considered in fundamental studies aiming to quantify the performance of UF and NC materials under irradiation.

It is generally accepted that sink efficiency of a grain boundary can be experimentally characterized by the formation of a defect denuded zone: a defect-free region near a grain boundary in an irradiated material [43,44]. Defect absorption by the grain boundaries results in the formation of a defect profile (defect densities increase as the distance from the grain boundary increases up to a bulk value) in the vicinity of the grain boundary. Such a profile is influenced by bulk defect mobilities. The denuded zone width is then the distance from the grain boundary where the defect concentration remains under a critical value, typically smaller than that necessary to nucleate larger-scale defects observable in transmission electron microscopy (TEM) [44]. An important implication of denuded zone formation reflected in the literature is that the higher the sink efficiency of the grain boundary, the larger the denuded zone that will form.

Denuded zone formation, however, can be condition dependent and may not be observed at particular irradiation conditions regardless of the grain boundary type and character [32,45]. Thus, several important questions arise: (1) Should every grain boundary have a denuded zone? (2) How do bulk defect (interstitials and vacancies) mobilities, extremely different in this material, affect denuded zone formation? (3) Is the denuded zone an unambiguous measure of sink efficiency? (4) Is the presence or absence of denuded zones a direct measure of enhanced radiation tolerance in nanostructured materials? (5) To what extent does sink efficiency reflect the role of grain boundaries in reducing irradiation damage?

In this work, we performed heavy ion and low-energy helium irradiation experiments on a materials system (tungsten) that possesses very distinct defect (vacancy and interstitial) mobilities at different irradiation conditions and damage regimes (displacement damage vs implanted damage) to answer the questions above. Heavy ion (Cu^+) irradiations were performed on coarse grain tungsten, labeled as CGW with an average grain size of a few μm , and UF/NC tungsten, labeled as NCW, where elongated nanocrystalline and ultra-fine grains coexist and the average grain size (shortest distance between two boundaries) ranges from 80 to a few hundred nm, at both room temperature (RT) and 1050 K using two different displacements per atom (dpa) values. Low-energy helium (2 and 4 keV) implantation was performed at RT, 773 K, and 1223 K. Dislocation-loop denuded zones were then investigated with TEM over a large number of grain boundaries in the two irradiated grades of W. Damage in the NCW and CGW was quantified considering both defect density and area. Finally, kinetic Monte Carlo simulations are performed to gain further insight into the physical origin of the defect profiles obtained experimentally. The primary conclusions are (1) Sink efficiency does not unambiguously describe the role of grain boundaries in reducing irradiation damage, (2) denuded zone formation is dependent on irradiation conditions and requires extra defect recombination at the grain boundaries, and (3) even when denuded zones do not form, grain boundaries can still act to store defects and contribute to the irradiation tolerance of nanocrystalline materials.

II. EXPERIMENTAL METHODOLOGY

A. Sample preparation

Two tungsten grades were investigated in this study: (1) a commercial tungsten grade provided by ESPI metals, USA, consisting of fine/coarse grain sizes (grains that are larger than 1 μm) and labeled as CGW; and (2) a NC (<100 nm) [13] and UF (100–500 nm) [12] tungsten grade (ultrafine and nanocrystalline grains coexist) which is labeled as NCW. The NCW grade was prepared via an orthogonal machining technique (preparation procedure is described elsewhere [46]). Both grades are high purity (nominally 99.95% and 99.99% for the NCW and the CGW, respectively).

TEM sample preparation of both grades was prepared via electropolishing a 100- μm -thick disk after mechanical polishing both sides to mirror finish. Electropolishing was performed with 0.5% NaOH solution at RT. The preparation process was previously detailed elsewhere [4]. The microstructure of the CGW has random distributions of low- and high-angle boundaries while the NCW grade is dominated by low-angle boundaries as determined previously by electron backscattered diffraction (EBSD) in a detailed study of loop and void damage under heavy ion irradiation [47]. TEM images and EBSD inverse-pole figure orientation maps showing the morphology and the texture of the pristine (prior to irradiation) samples are given in Ref. [47].

B. Irradiation

Ex situ heavy ion irradiation of the samples was performed in the Ion Beam Materials Laboratory (IBML) at Los Alamos National Laboratory (LANL) using the Tandem beam with 3-MeV Cu^+ ions at nominal incidence. The displacement per atom (dpa) rates were 0.0167 and 0.000 167 dpa/s. Irradiation was performed at two different temperatures (RT and 1050 K). The samples were irradiated to different dpa values ranging from 0.2 to 4 dpa. To determine the dpa and the dpa rate, the Kinchin-Pease model in the stopping range of ions in matter (SRIM) Monte Carlo computer code (version 2013) [48] was used to determine the damage per incident ion (which was 0.76 vacancy/ion/Å) in 100-nm sample thickness. Next, 4-keV normal-incidence helium ion irradiation at RT and 773 K were performed using the neutron irradiation material ion implantation experiment (NIMIIX), at Idaho National Laboratory, with an average ion dose of $3.46 \times 10^{17} \text{ m}^{-2} \text{ s}^{-1}$, a total dose of $2.14 \times 10^{20} \text{ m}^{-2}$, and a corresponding peak dose of 0.91 dpa. Then 2-keV helium irradiation was performed at 1223 K *in situ* in the JEOL JEM-2000FX TEM at the Microscope and Ion Accelerator for Materials Investigations (MIAMI) facility at the University of Huddersfield [49]. The dose rate and the final dose were $1.73 \times 10^{17} \text{ m}^{-2} \text{ s}^{-1}$ and $3.2 \times 10^{20} \text{ m}^{-2}$, respectively, and the peak dpa was ~ 1.1 dpa. In all calculations, 40 eV was assumed to be the displacement threshold in tungsten [50]. The ion distributions, dpa profiles (Fig. S1), and dpa calculations are illustrated in the Supplemental Material [51].

C. Characterization and quantification

The irradiated samples were characterized via TEM using an FEI-Technai-G2-F30 transmission electron microscope

with electron beam energies of 300 keV in the Electron Microscopy Laboratory (EML) at LANL. Processing of images was performed using the IMAGE J software [52]. Quantification of the irradiation was performed using two beam conditions with the g -vector along (1-10) or (200). The quantification considered the overall damage (product of loop density and loop size). All dislocation loops (of both interstitial and vacancy type) were considered. When comparing the size of the loops, the $g \cdot b$ values were the same for both samples.

Grains used in quantifying the resulting damage were taken from neighboring regions in the sample (to minimize any discrepancy in the foil thickness).

D. Simulations

To further understand the role of defect properties on the experimentally obtained defect denuded zones, kinetic Monte Carlo simulations with saturable boundaries were performed. Whether grain boundaries are saturable or not is still the subject of debate in the literature; we assume saturable boundaries based on our previous studies of defect-boundary interactions [20,34,35]. Further, the model used here, based on saturable boundaries, is able to explain our experimental observations, as discussed below. That said, the true behavior of defects at grain boundaries requires further study and direct experimental validation.

The kinetic Monte Carlo (KMC) [53–55] algorithm solves the dynamic evolution of a Markovian process provided that the probabilities per unit time of the possible events are first order in time. This methodology has been extensively used to study radiation damage by following the irradiation-induced defects as they are formed and diffuse in the system ([56], and references therein). Figure 1(a) shows the physical model that we simulate with KMC in this work. Vacancies (Vs) and self-interstitials (SIs) are created at a given dose rate. They can diffuse on an underlying lattice with a rate calculated via harmonic transition state theory [57] knowing the migration barrier and assuming a constant prefactor equal to 10^{12} s^{-1} . Vacancies and SIs can recombine if they are at a first nearest neighbor (1nn) distance. An interface is modeled in the system as a region in space where the equilibrium and diffusion properties of the defects are different from bulk. The elastic interaction that might exist between defects and the interface is not taken into account. Though such interactions might slightly change the predicted defect profiles [58], possibly leading to a difference in the timescale of the process, they will not modify the main conclusions of this study. Figure 1(b) shows a schematic of the different landscapes that describe the thermodynamics and kinetics of V and SI in the model. The primary goal of the model is to qualitatively assess how defect profiles change under different irradiation conditions or as the different materials properties are modified.

As mentioned, a critical parameter that has been traditionally used to assess the effect of an interface on defect profiles is the sink efficiency. The sink efficiency is defined as follows [59]:

$$\eta = \frac{J_{\text{Interface}}^{\alpha}}{J_{\text{Perfect}}^{\alpha}}, \quad (1)$$

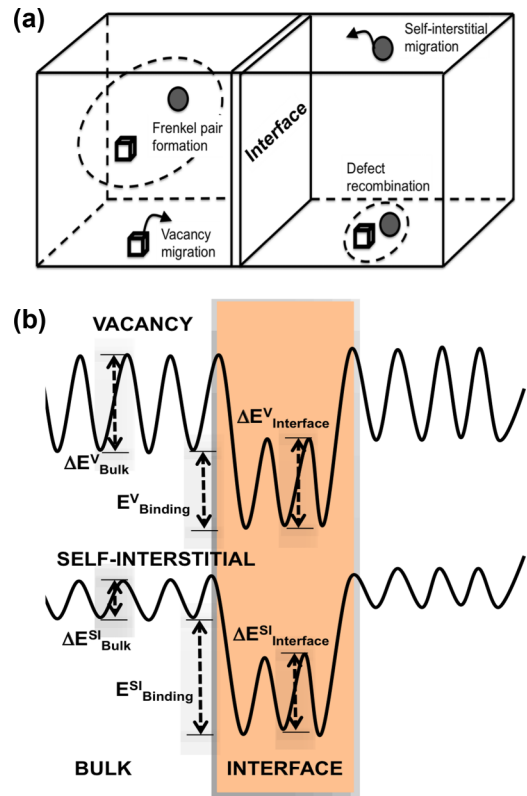


FIG. 1. (a) Schematic of the physical model to be solved using the KMC algorithm. (b) Schematic landscapes for the thermodynamic and kinetic energetics for both Vs and SIs in bulk and at the grain boundary. The width of the interface is larger than one plane to allow for defect migration within the boundary for this specific sample oriented in the [100], [010], and [001] directions. However, elastic interactions extending into the grain itself are neglected in this model.

where $J_{\text{Interface}}^{\alpha}$ is the flux of defect α into the interface under consideration and $J_{\text{Perfect}}^{\alpha}$ is the flux of defects into a perfect sink, where a perfect sink is one that maintains the equilibrium concentration of defects at its boundary. Because that equilibrium concentration of defects is negligible compared to the amount of irradiation-induced defects, we have considered this equilibrium concentration to be zero.

An energy landscape like that shown in Fig. 1(b) was assigned for Vs and SIs. The migration barriers in bulk were $\Delta E_{\text{bulk}}^{\text{V}} = 1.667 \text{ eV}$ and $\Delta E_{\text{bulk}}^{\text{SI}} = 0.054 \text{ eV}$ for V and SIs, respectively [60,61]. A dose rate of 10^{-4} dpa/s , corresponding to the higher-flux experiments, was simulated at a temperature of 1050 K. An attractive binding energy of defects to the grain boundary of $E_{\text{binding}}^{\text{SI}} = 1.5 \text{ eV}$ and $E_{\text{binding}}^{\text{V}} = 1.0 \text{ eV}$ for SIs and Vs was assumed. Vacancy mobility at the boundary was taken to be the same as in bulk although a migration barrier of $\Delta E_{\text{Interface}}^{\text{SI}} = 0.554 \text{ eV}$ was employed for self-interstitials. These numbers do not represent any specific boundary but are taken as variable parameters, and, along with the defect migration energies in bulk, were varied to mimic different irradiation conditions.

Although the great disparity in migration barriers between defects makes the problem numerically stiff, we were able to extend most of our simulations up to steady state. Irradiation

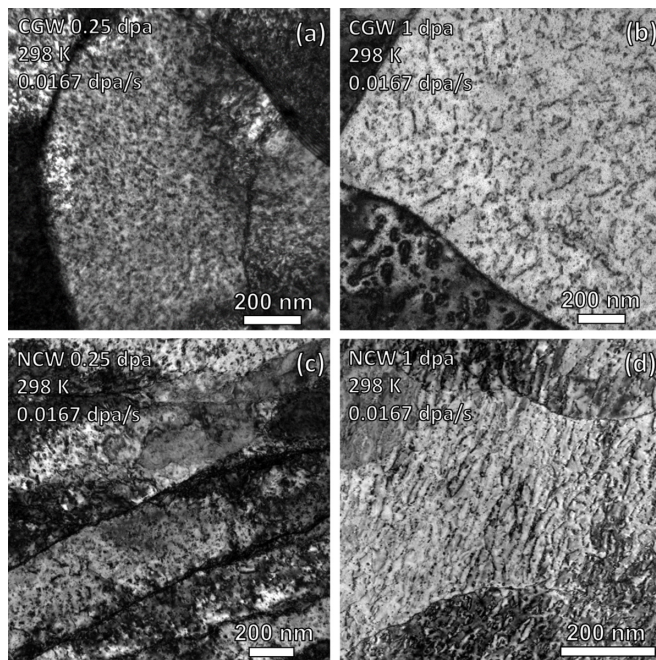


FIG. 2. Bright-field TEM images of 3-MeV Cu^+ irradiated CGW and NCW grades with a dose rate of 0.0167 dpa/s at 298 K showing no denuded zone formation. (a),(b) CGW grade at 0.25 and 1 dpa, respectively. (c),(d) NCW grade for 0.25 and 1 dpa, respectively.

was mimicked by inserting Frenkel pairs in the sample at the prescribed dose rate. Thus, no cascade effects were considered in this study. Also, defect clustering was neglected. The main goal of the simulations was to understand general trends, not a quantitative description of the microstructure evolution; i.e., we wanted to understand the main effect of the dissimilar defect properties in the defect concentration profile as an observable of interest linked to the defect denuded zone measured experimentally.

III. RESULTS

Irradiation of the samples was performed at RT and 1050 K to examine the effect of temperature on denuded zone formation. As described above, SI and V mobilities are remarkably different [60,61]. According to positron annihilation studies in tungsten, monovacancies can migrate at temperatures over 523 K while vacancy clusters migrate at higher temperatures (over 773 K) [62]. Therefore, the experimental conditions chosen in this work were designed to enable vacancy migration at one temperature and inhibit it at another temperature, while interstitial migration can occur at both temperatures.

The morphology of the heavy ion irradiated samples for different doses at RT and 1050 K using a dose rate of 0.0167 dpa/s is shown in Figs. 2 and 3. Even at low doses (approximately 0.25 dpa), no denuded zones were observed in either the NCW or the CGW grades at either temperature. The dose rate was then reduced to 0.000167 dpa/s (100 times less than the initial dose rate), to investigate flux effects on the damage evolution. Figures 4 and 5 show the morphology of the irradiated samples at low dose rate using the same irradiation temperatures as in the initial (high dose rate) set

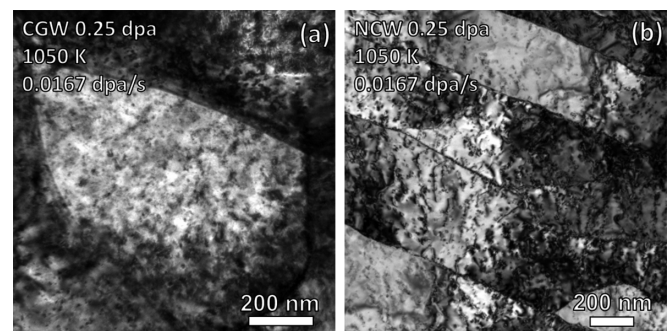


FIG. 3. Bright-field TEM images of 3-MeV Cu^+ irradiated CGW and NCW grades with a dose rate of 0.0167 dpa/s at 1050 K showing no denuded zone formation. (a) CGW grade at 0.25 dpa (b) NCW grade at 0.25 dpa.

of experiments. Although the damage is lower in this case, as defects have more time to interact and annihilate or reach the interfaces, the grain boundaries in both NCW and CGW do not exhibit any denuded zones. All figures were chosen to emphasize defect structures near the grain boundaries and are not intended to compare irradiation damage in the different samples (which is diffraction contrast dependent).

Since no denuded zones are formed in any of the heavy ion irradiations, any effect of grain boundaries on defect absorption at both temperatures should be evaluated via quantification of the total damage. Dislocation-loop density alone is not sufficient to quantify damage. Rather, one needs to also account for the size of loops to obtain an integrated number of defects within the material. Therefore, the overall damage quantified in this work at 0.25 dpa (using the lower

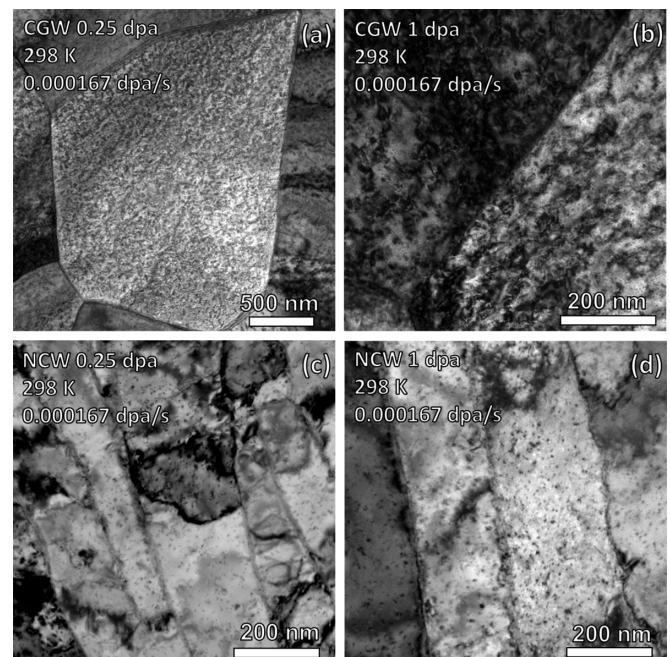


FIG. 4. Bright-field TEM images of 3-MeV Cu^+ irradiated CGW and NCW grades with a dose rate of 0.000167 dpa/s at 298 K showing no denuded zone formation. (a),(b) CGW grade at 0.25 and 1 dpa, respectively. (c),(d) NCW grade for 0.25 and 1 dpa, respectively.

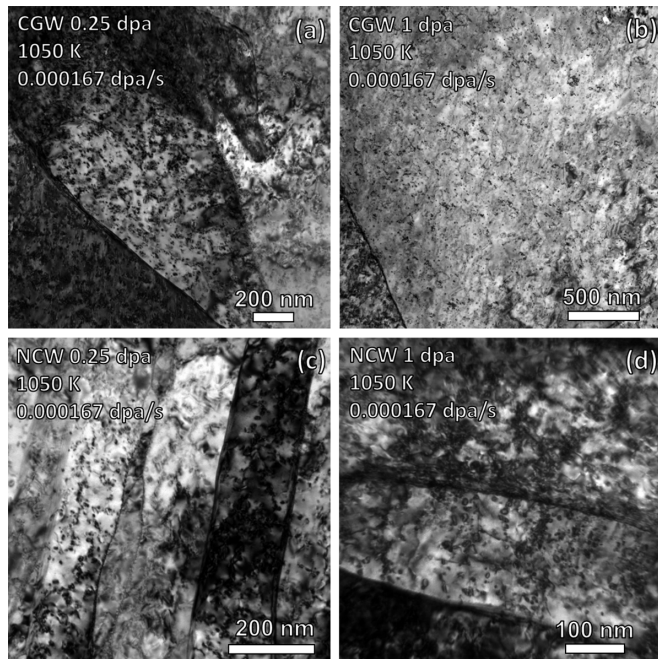


FIG. 5. Bright-field TEM images of 3-MeV Cu^+ irradiated CGW and NCW grades with a dose rate of 0.000 167 dpa/s at 1050 K showing no denuded zone formation. (a),(b) CGW grade at 0.25 and 1 dpa, respectively. (c),(d) NCW grade for 0.25 and 1 dpa, respectively.

dpa rate of 0.000 167 dpa/s) took into account both loop density and sizes (loop planar area). Both loop density and sizes are also dependent on the diffraction conditions ($\mathbf{g}\cdot\mathbf{b}$ contrast). To compare the damage in irradiated NCW vs CGW, we used two beam conditions with the assumption that both irradiated grades have similar types of loops. In NCW, where grain sizes were about 150–200 nm, tilting from one g -vector to another is very challenging. Therefore, we compare the damage in NCW and CGW using different NCW grains with diffraction conditions ($\mathbf{g}\cdot\mathbf{b}$) that matched the quantified CGW grain. That is, rather than trying to tilt the sample to align the g -vector, we simply chose grains that were aligned as loaded with similar g -vectors to the grains in the CGW samples. The result of this quantification is shown in Fig. 6. The NCW

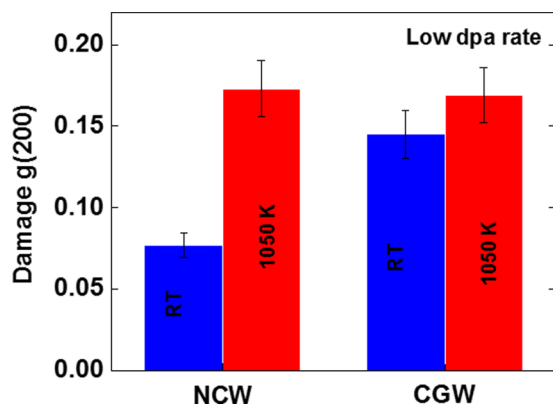


FIG. 6. Dislocation-loop damage quantification in the 3-MeV Cu^+ irradiated CGW and NCW at 0.25 dpa [47].

showed less loop damage at RT but similar loop damage at 1050 K. However, the NCW showed less void damage at high temperature than the CGW [47] which can evolve from vacancy type loops [63,64]. Therefore, if voids that are evolved from vacancy type loops are considered, the total loop damage in the NCW should be less than the CGW. Moreover, surface effects [65] (proximity to the surface), which lead to loop annihilation through interaction with the surface, are much larger in the CGW since the grain boundary to surface area ratio (calculated from TEM images) was 0.04 in the CGW grade compared to 0.46 in the NCW grade; thus more loops and interstitials can be annihilated by the surface during irradiation in the case of CGW.

Implantation of helium can affect denuded zone formation. For example, Zhang *et al.* [66] observed denuded zones (of interstitial loops) in tungsten at 573 K in a dual beam irradiation experiment where self-ions and helium ions were implanted in tungsten. In order to gain insight into the similarities and differences between irradiation conditions, we performed a second series of experiments in which we implanted helium in the NCW grade to examine the effect of helium on denuded zone formation in tungsten. Three temperatures were chosen: (1) RT where vacancies do not migrate, (2) 773 K where vacancies can migrate but vacancy complexes and helium-vacancy complexes do not, and (3) 1223 K where vacancies, vacancy clusters, and helium-vacancy-rich complexes can migrate [67]. The morphologies of the helium-implanted samples implanted are shown in Fig. 7. At RT, no denuded zones were observed. However, at 773 and 1223 K, denuded zones were indeed observed. While some grains showed denuded zone formation, others did not, suggesting an overall effect of the grain boundary character [43] or possible denuded zone collapse. Denuded zone formation for all of the experimental conditions is summarized in Table I.

IV. DISCUSSION

A. Sink efficiency

The sink efficiency of a grain boundary is often correlated to the width of the denuded zone. Beyerlein *et al.* [43] derived the following equation at steady state using kinetic rate theory, under the assumption that defect recombination could be treated as a background annihilation rate (where we have expressed this for interstitials as we are interested in denuded zones of interstitial loops):

$$\lambda_{\text{DZ}} \sqrt{\frac{K_{\text{si}}}{D_i}} = \ln \eta_i - \ln \left(1 - \Delta c_i \frac{K_{\text{si}}}{K_0} \right). \quad (2)$$

Here, λ_{DZ} is the width of the denuded zone, K_{si} is the interstitial-sink reaction rate coefficient (including interstitial-vacancy (I-V) recombination), K_0 is the defect production rate, D_i is the interstitial diffusivity, Δc_i is the excess interstitial concentration at which loops are expected to form, and η_i is the sink efficiency of interfaces and grain boundaries for interstitials, as defined in Eq. (1). η_i can range from 0 (no interstitial absorption/interaction) to 1 (perfect sink). Note that a more complete model that explicitly accounts for both interstitials and vacancies and thus I-V recombination gives

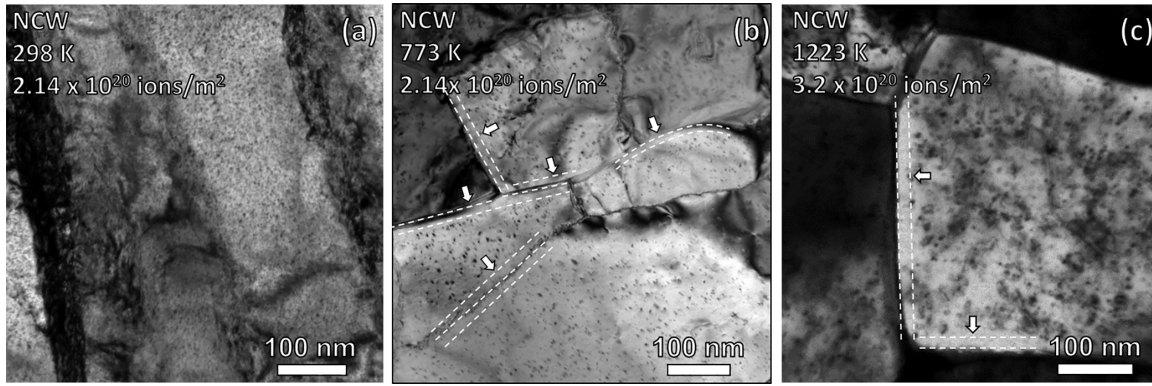


FIG. 7. Bright-field TEM images of helium ion (implanted damage) implanted NCW grade. (a) 4-keV implantation at 298 K and final fluence of $2.14 \times 10^{20} \text{ m}^{-2}$ showing no denuded zone formation. (b) 4-keV implantation at 773 K and final fluence of $2.14 \times 10^{20} \text{ m}^{-2}$ showing denuded zone formation (denuded grain boundaries pointed by arrows). (c) 2-keV implantation at 1223 K and final fluence of $3.2 \times 10^{20} \text{ m}^{-2}$ showing denuded zone formation (denuded grain boundaries indicated by arrows).

qualitatively different solutions [68]. That said, this simpler one-defect model describes the salient behavior of the system.

As mentioned, it is typically assumed that denuded zones are a direct measure of the sink efficiency of a boundary. Certainly, Eq. (1) implies a direct relationship. However, it further shows that the denuded zone width also depends on the bulk recombination processes. In particular, one can imagine setting $\lambda_{\text{DZ}} = 0$ in Eq. (1) and solving for η_i :

$$\eta_i = 1 - \Delta c_i \frac{K_{\text{si}}}{K_0}. \quad (3)$$

This result implies that, even when there is no apparent denuded zone (i.e., $\lambda = 0$), the sink efficiency of the interfaces can be nonzero (i.e., $\eta \neq 0$) and have an impact on the damage evolution. What this means, physically, is a bit vague. It could be that defect concentrations all the way to the interface are higher than the critical concentration so no denuded zone is apparent. Alternatively, the concentrations could be lower everywhere than the critical concentration. More important than this relationship, however, is the clear implication that interfaces may be acting as sinks and affecting defect populations even if no denuded zone forms. This is consistent with our experimental results that show that, while neither set of damaged samples (as opposed to implanted) exhibits denuded zones, the NCW samples contain less overall damage than the CGW samples, at least at low temperature. However, this argument is only suggestive. Further insight is gained

from KMC simulations of the damage evolution in these materials.

B. Heavy ion irradiation (displacement damage)

Our KMC model was used to obtain deeper understanding on the defect profiles and the reason why no denuded zones were observed under the heavy ion irradiation conditions. We ran simulations at 400 and 1050 K and a dose rate of 10^{-4} dpa/s . Figures 8(a) and 8(c) show the defect concentration profiles at steady state. We observe that both profiles are nearly flat. Even at elevated temperature, the disparity in defect mobilities allows for self-interstitials to explore the whole landscape before recombining with vacancies, which leads to the flat profile shown in the figure. Figures 8(b) and 8(d) show the recombination probability as a function of the position normal to the interface. We note that the probability is fairly uniform. At 1050 K there is a small bump at the interface, denoting a slightly larger recombination tendency at that point. Without extra annihilation at the interface, there is no net flux of defects toward the interface, which would correlate to a negligible sink efficiency.

C. Effect of vacancy migration and self-interstitial binding energy to the interface

We hypothesize that the flat profiles shown above are a consequence of the disparity in mobilities of the single defects,

TABLE I. Grain boundary denuded zone presence/absence at different irradiation conditions on tungsten.

	Condition	Temperature	Denuded
Displacement damage	0.25 and 1 dpa (low dpa rate)	298 K	No
	0.25 and 1 dpa (low dpa rate)	1050 K	No
	0.25 and 1 dpa (high dpa rate)	298 K	No
	0.25 (high dpa rate)	1050 K	No
He implantation damage	$2.14 \times 10^{20} \text{ ions/m}^2$	298 K	No
	$2.14 \times 10^{20} \text{ ions/m}^2$	773 K	Yes
	$3.2 \times 10^{20} \text{ ions/m}^2$	1223 K	Yes

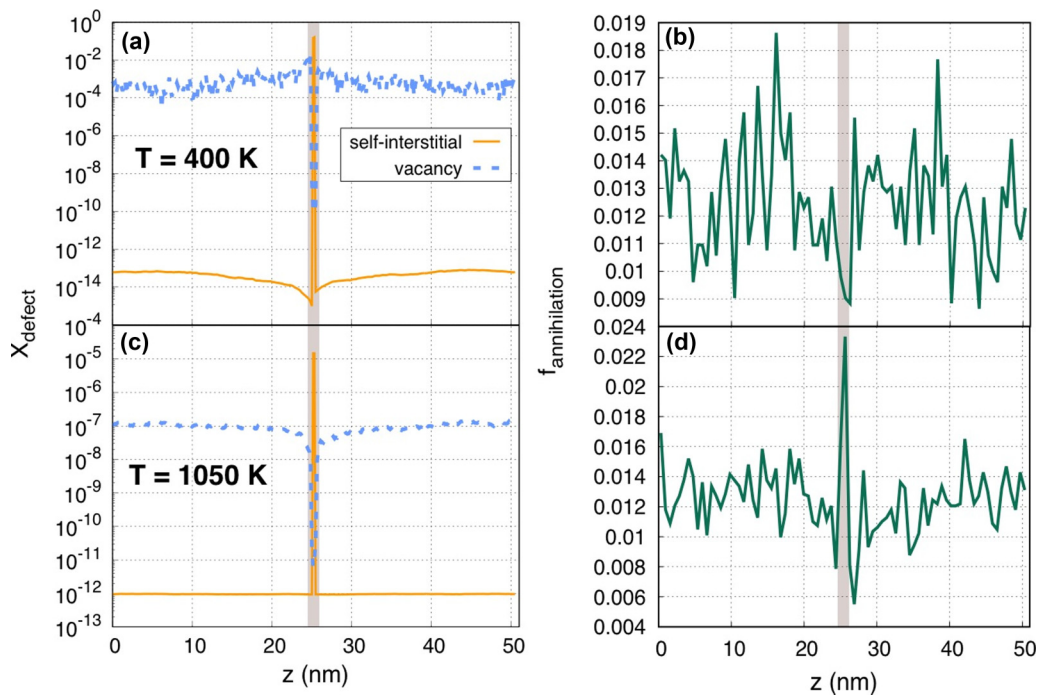


FIG. 8. Self-interstitial and vacancy concentration profiles at steady state as given by the KMC model at (a) 400 K and (c) 1050 K. Recombination probability as a function of the position normal to the interface at (b) 400 K and (d) 1050 K.

which allows the SIs to explore the whole landscape before recombining with Vs. Thus, the recombination probability remains homogeneous in the system. To test this hypothesis we have run simulations in which the mobility of the vacancies is made equal to the mobility of self-interstitials in both bulk and grain boundary. The results are shown in Figs. 9(a), 9(c), where we see that the profiles now exhibit some spatial dependence with distance from the grain boundary. These nonflat profiles could lead to denuded zones. We see in Fig. 9(c) the recombination probability. In this case we observe that defects recombine preferentially at the interface, which leads to defect fluxes toward the sink.

Alternatively, we have also tested the effect of the binding energy of the SIs to the interface on the concentration profiles. Increasing the binding energy (but leaving the mobilities at their original values) increases the residence time of interstitials at the boundary, which in turn enhances the recombination probability at the sink. Figures 9(b), 9(d) show the results of having a 2-eV binding energy for interstitials to be attracted to the interface. We notice that the SI profile is indeed nonflat, denoting a flux of defects toward the interface. This is clearly seen in the annihilation probability distribution [Fig. 9(d)] with much larger recombination taking place at the interface. The reduced vacancy mobility makes it difficult to reach steady state in this case. That is the reason we observe an asymmetric vacancy profile in Fig. 9(b).

D. Effect of helium implantation

Our experiments reveal that the implantation of He leads to dislocation-loop denuded zones near grain boundaries. We hypothesize here that the main effect of He is to slow down self-interstitials. Slowing down of self-interstitials by

He has been observed in atomistic simulations using empirical potentials and density functional theory [69,70]. These studies find that the self-interstitial migration energy increases to up to ~ 1 eV as self-interstitials bind to interstitial He atoms. Accordingly, we have increased the self-interstitial migration barrier to 1.5 eV (to exacerbate the effect) in our simulations while leaving the rest of the parameters equal. Figure 10 shows the results of these simulations, where we show the defect profiles [Fig. 10(a)] and the recombination probability [Fig. 10(b)]. We observe that the defect concentration profiles exhibit a curvature that leads to a net flux of defects toward the interface. As we see in Fig. 10(b), the net flux of defects is induced by the extra recombination probability at the interface. Furthermore, the curved profiles are the basis for the formation of denuded zones as the clustering probability depends quadratically on the defect concentration. We note that, in this last case, when self-interstitial mobility is low, the concentration of self-interstitials is much larger than when their mobility is faster. We acknowledge then that the choice of threshold concentration will play an important role in determining whether a denuded zone will be formed or not.

E. Implications of experimental observations and modeling results

The key summary of both modeling and experiments is that the recombination probability of SIs and Vs has to be larger at the interface for denuded zones to form. In the case that the defect mobilities are significantly different, the fast species might have time to explore the whole landscape before the slow species reaches the sink. If that is the case, flat profiles develop and the sink efficiency of the interface is negligible.

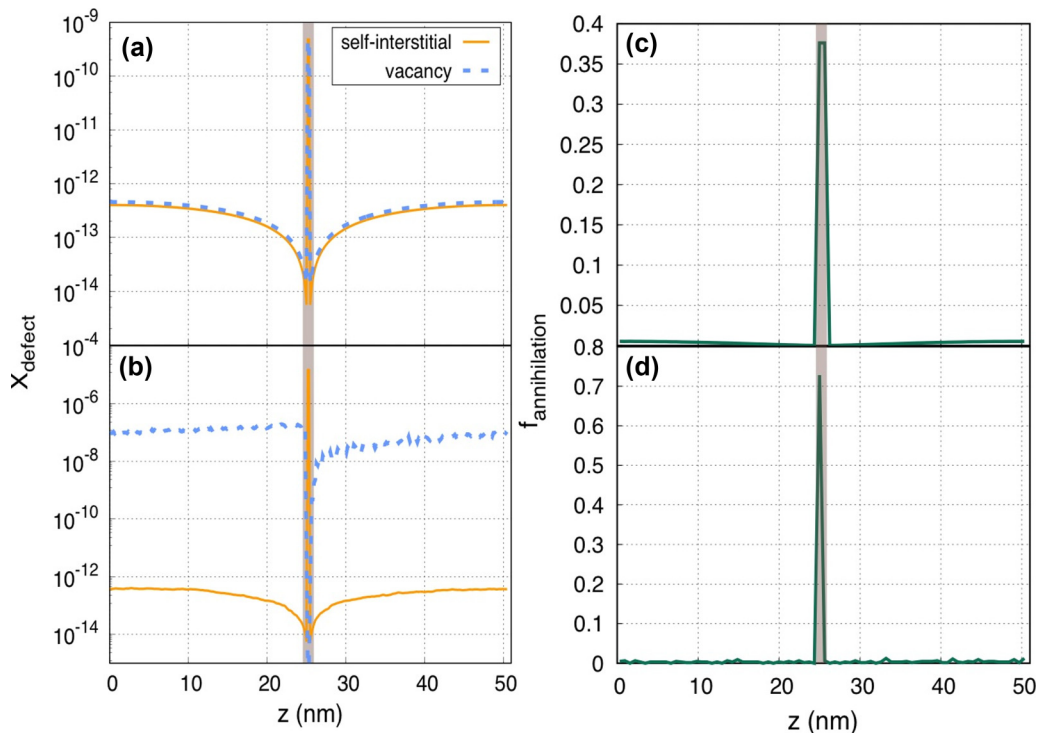


FIG. 9. (a) Self-interstitial and vacancy concentration profiles at steady state as given by the KMC model for (a) fast vacancies and (b) 2.0 eV SI binding energy to the interface. Recombination probability as a function of the position normal to the interface for (c) fast vacancies and (d) 2.0 eV SI binding energy to the interface. The simulations were performed at 1050 K.

On the other hand, if the fast species spends most of the time at the interface (if the defect-interface binding energy is large) and allows for the slow defect to reach it, recombination at the interface will be promoted and concentration profiles will develop, leading to denuded zones. For these effects to happen, the sink needs to be saturable, i.e., defects do not annihilate at the sink and there is a finite probability of reemission to the grain. If boundaries were able to annihilate defects without recombination, concentration profiles would always develop and perfectly flat profiles could not be attained, in contrast to what we observed in the pure damage experiments.

It is also important to note that the sink efficiency [Eq. (1)] does not represent a property of a grain boundary but of a particular diffusion equation [43]. The additive nature of the different defect fluxes involved in this diffusion equation leads to the fact that the ratio of the defect fluxes toward the actual boundary over the defect fluxes toward an idealized boundary depends also on the properties of the defects in bulk. That is, the same grain boundary embedded in grains with different conditions (orientation, defect mobilities, loop density, etc.) will result in different sink efficiencies. This can be readily seen from Eq. (1), where the sink efficiency can be obtained as a function of defect mobilities (D_i) and the rate of defect annihilation (K_{si}). Furthermore, we demonstrate that saturable boundaries with zero sink efficiency might lead to a total decrease of defects in the bulk at steady-state since they can act as storage for defects. The storage capacity will directly depend on the properties of defects at the boundary, such as the binding energy of defects to the interface and the mobility of the defects inside the boundary. The higher the binding energy the more defects could be stored at the interface.

The main hypothesis in the use of the sink efficiency to characterize the behavior of an interface under irradiation is that the boundary itself will be able to maintain a constant sink efficiency independently of the external conditions. That is, it will modify the properties of the defects within the interface such that the changes in fluxes due to any variation within the grain will be accompanied by changes inside the boundary to maintain the sink efficiency. However, atomistic simulations [71,72] do not indicate that the changes in defect properties within a loaded boundary will result in a constant sink efficiency (they might not indicate that the boundary is saturable either). We have considered here that the properties of defects at the interface are more fundamental quantities than the sink efficiency such that we did not enforce the sink efficiency to be constant. On the other hand, we have seen that properties in the bulk play a significant role on the defect profiles developed under irradiation. That is a strong indication that the definition of the sink efficiency is tied to a specific diffusion equation, in which all the terms play a role, and not so much to a certain boundary; i.e., the sink efficiency should be taken as a boundary condition for the diffusion equation and cannot be directly linked to a certain boundary as a fixed property.

Figure 11 shows the average concentration of SI in bulk (far from the interface) depending on the grain size. In general, with the model that we are using here, the SI concentration increases as grain sizes increase, for a given production rate. These results come from two effects, the enhanced recombination in small systems due to correlation effects and storage of defects at the interface. Therefore, we can conclude that the nanocrystalline systems will improve radiation tolerance even

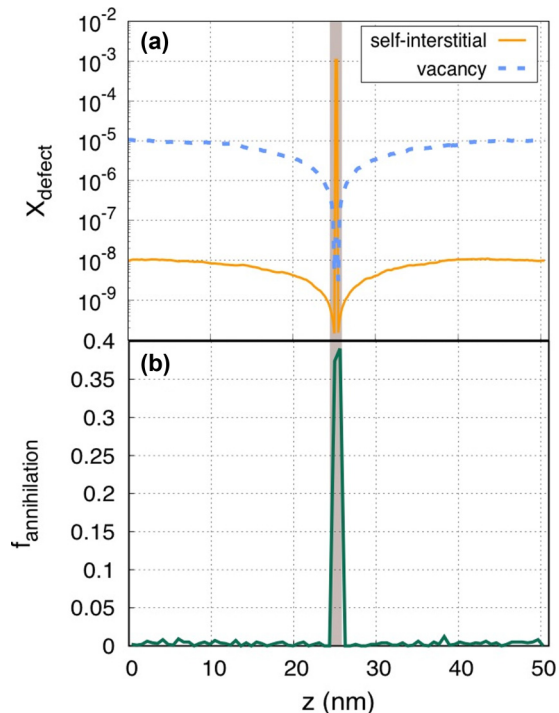


FIG. 10. (a) Self-interstitial and vacancy concentration profiles at steady state as given by the KMC model for slow interstitials. (b) Recombination probability as a function of the position normal to the interface. The simulations were performed at 1050 K.

in specific situations in which the grain boundaries are not strong sinks for defects (i.e., no denuded zones are formed).

An important point to discuss regards the sessile loops that are formed directly from the collision cascades and their effect on the loop density profiles and denuded zone formation. Setyawan *et al.* [73] have shown, through molecular dynamics simulations, that vacancy loops of $\langle 100 \rangle$ type can form in higher-energy cascades. Experimentally, Yi *et al.* [74] have seen only 10% of the loops are $\langle 100 \rangle$ loops at 1023 K with 2 MeV self-ion irradiation in tungsten. Yi *et al.* argued that the $\langle 100 \rangle$ loops are not stable at higher temperatures. For the Cu^+ irradiated samples (this work), it was observed that at 0.25 dpa $\sim 50\%$ of the loops are of $\langle 100 \rangle$ type which are deduced

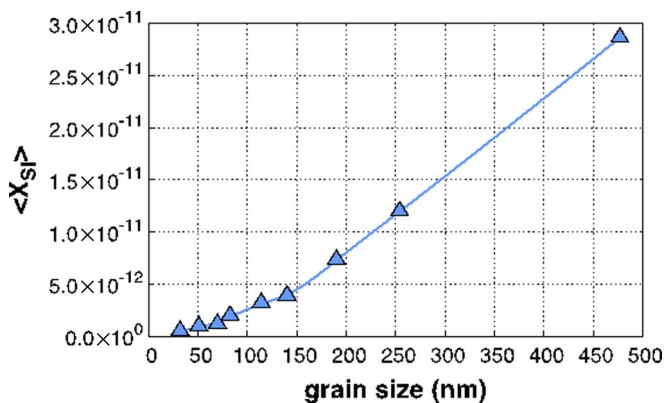


FIG. 11. Average concentration of SI in bulk depending on grain size. The simulations were performed at 1050 K.

(based on loop-size analysis) to be of $\langle 100 \rangle$ vacancy type [47]. The $\langle 100 \rangle$ loops are relatively sessile compared to the glissile $\langle 111 \rangle$ loops. However, not all loops formed are of this type. If only $\langle 100 \rangle$ loops are formed in the vicinity of the grain boundaries directly from the cascade, while both $\langle 100 \rangle$ and $\langle 111 \rangle$ loops are formed in the grain interior, a loop density profile would exist across the grain boundary to the grain matrix, which is not the case in this work [e.g., Fig. 3(d)]. Moreover, loops formed directly from the cascade are usually small; however, loops observed near the grain boundaries in this work (e.g., Fig. 3) are relatively large indicating their growth via interstitial absorption. In addition, self-ion irradiation experiments on iron showed denuded zone formation despite having $\langle 100 \rangle$ loops dominate at high temperatures [75], unlike the case in this work where denuded zones are not formed.

V. CONCLUSIONS

The performance of nanocrystalline materials in extreme irradiation environments can be evaluated only after understanding and quantifying the role of grain boundaries in mitigating irradiation damage. While the role of individual grain boundaries has been shown to depend on their overall character, their sink efficiency is often characterized by the formation of denuded zones in their vicinity. However, answers for several outstanding and puzzling questions regarding denuded zone formation, grain boundary sink efficiency, and the correlation between both, are still lacking. By performing a combined experimental (displacement and implanted irradiations at different conditions) and modeling (KMC) research effort targeted on a common material system (nanocrystalline and coarse grain tungsten) with distinct defect (interstitial and vacancy) mobilities, insights on denuded zone formation, and the sink efficiency of the grain boundary are reached and summarized as follows:

(1) The relationship between denuded zone width and sink efficiency is not 1:1. Most importantly, the sink efficiency is not an intrinsic property of a given grain boundary, but also depends on other factors not relating to the grain boundary itself, such as the defect recombination rates in the grain interior. The sink efficiency is defined as the ratio between the fluxes of defects toward the real boundary over the fluxes of defects to the ideal version of such boundary. The additive nature of the fluxes in the diffusion equation makes that ratio change if any of the bulk conditions change. That is, the same boundary inside different crystals with different sink densities or different diffusivities (for example) will show different sink efficiencies.

(2) Denuded zones will only form at grain boundaries if there is extra recombination at the grain boundary, whether intrinsic annihilation at the sink or enhanced I-V recombination due to excess defect concentrations.

(3) The extent to which this enhanced I-V recombination occurs is critically dependent on the disparity between defect mobilities. The smaller the difference, the greater the recombination and the larger the potential denuded zone. This would mean that denuded zone formation would not occur when vacancy migration does not occur or when the vacancy and interstitial mobilities (temperature dependent) are very distinct.

(4) If grain boundaries become saturated, the sink efficiency becomes zero and the defect profiles become flat, with no formation of denuded zones.

(5) Even if this happens, even if grain boundaries have zero sink efficiency, they still modify the defect concentrations in the bulk through a storage effect, and either increasing the density of grain boundaries and/or the storage capacity of individual grain boundaries (through the binding energy) will increase this storage effect and reduce the total defect content in the grain interiors.

Considering all the points above, a conclusion can be reached that sink efficiency does not describe unambiguously the role of grain boundaries in limiting irradiation damage in nanocrystalline materials. The unique insights summarized in this work should refine the understanding of the role of grain boundaries in nanocrystalline materials exposed to extreme irradiation conditions and the evaluation of their performance.

ACKNOWLEDGMENTS

Research presented in this article was also supported by the Laboratory Directed Research and Development program of Los Alamos National Laboratory under Project No. 20160674PRD3. We gratefully acknowledge the support of the U.S. Department of Energy through the LANL/LDRD Program and the G. T. Seaborg Institute for this work. B.P.U. and E.M. acknowledge support by the U.S. Department of Energy, Office of Science, Office of Fusion Energy Sciences, and Office of Advanced Scientific Computing Research through the Scientific Discovery through Advanced Computing (SciDAC) project on Plasma–Surface Interactions under Award No. DE-SC0008875. The authors would like to acknowledge the MIAMI facility’s scientists and staff at the University of Huddersfield for performing the 2 keV helium implantation, and Matt Chancey for the help with the heavy ion irradiation.

-
- [1] J. Hemminger, G. Fleming, and M. Ratner, Directing matter and energy: Five challenges for science and the imagination, Department of Energy’s Office of Science Report, 2007 (unpublished); https://science.energy.gov/~media/bes/pdf/reports/files/Directing_Matter_and_Energy_rpt.pdf.
- [2] R. W. Grimes, R. J. Konings, and L. Edwards, Greater tolerance for nuclear materials, *Nat. Mater.* **7**, 683 (2008).
- [3] J. Knaster, A. Moeslang, and T. Muroga, Materials research for fusion, *Nat. Phys.* **12**, 424 (2016).
- [4] O. El-Atwani, J. Hinks, G. Greaves, S. Gonderman, T. Qiu, M. Efe, and J. Allain, In-situ TEM observation of the response of ultrafine-and nanocrystalline-grained tungsten to extreme irradiation environments, *Sci. Rep.* **4**, 4716 (2014).
- [5] F. Ferroni, X. Yi, K. Arakawa, S. P. Fitzgerald, P. D. Edmondson, and S. G. Roberts, High temperature annealing of ion irradiated tungsten, *Acta Mater.* **90**, 380 (2015).
- [6] S. Kajita, W. Sakaguchi, N. Ohno, N. Yoshida, and T. Saeki, Formation process of tungsten nanostructure by the exposure to helium plasma under fusion relevant plasma conditions, *Nucl. Fusion* **49**, 095005 (2009).
- [7] O. El-Atwani, M. Efe, B. Heim, and J. P. Allain, Surface damage in ultrafine and multimodal grained tungsten materials induced by low energy helium irradiation, *J. Nucl. Mater.* **434**, 170 (2013).
- [8] M. J. Baldwin, and R. P. Doerner, Formation of helium induced nanostructure ‘fuzz’ on various tungsten grades, *J. Nucl. Mater.* **404**, 165 (2010).
- [9] S. J. Zinkle and G. Was, Materials challenges in nuclear energy, *Acta Mater.* **61**, 735 (2013).
- [10] E. Aydogan, S. Maloy, O. Anderoglu, C. Sun, J. Gigax, L. Shao, F. Garner, I. Anderson, and J. Lewandowski, Effect of tube processing methods on microstructure, mechanical properties and irradiation response of 14YWT nanostructured ferritic alloys, *Acta Mater.* **134**, 116 (2017).
- [11] P. Lapouge, F. Onimus, M. Coulombier, J.-P. Raskin, T. Pardoën, and Y. Bréchet, Creep behavior of submicron copper films under irradiation, *Acta Mater.* **131**, 77 (2017).
- [12] Q. Wei, T. Jiao, K. Ramesh, E. Ma, L. Kecskes, L. Magness, R. Dowding, V. Kazykhanov, and R. Valiev, Mechanical behavior and dynamic failure of high-strength ultrafine grained tungsten under uniaxial compression, *Acta Mater.* **54**, 77 (2006).
- [13] Q. Wei, H. Zhang, B. Schuster, K. Ramesh, R. Valiev, L. Kecskes, R. Dowding, L. Magness, and K. Cho, Microstructure and mechanical properties of super-strong nanocrystalline tungsten processed by high-pressure torsion, *Acta Mater.* **54**, 4079 (2006).
- [14] Y. Wang, M. Chen, F. Zhou, and E. Ma, High tensile ductility in a nanostructured metal, *Nature* **419**, 912 (2002).
- [15] M. L. Jenkins and M. A. Kirk, *Characterisation of Radiation Damage by Transmission Electron Microscopy* (CRC Press, Boca Raton, FL, 2000).
- [16] W. Han, M. Demkowicz, E. Fu, Y. Wang, and A. Misra, Effect of grain boundary character on sink efficiency, *Acta Mater.* **60**, 6341 (2012).
- [17] O. El-Atwani, A. Suslova, T. Novakowski, K. Hattar, M. Efe, S. Harilal, and A. Hassanein, In-situ TEM/heavy ion irradiation on ultrafine-and nanocrystalline-grained tungsten: Effect of 3 MeV Si, Cu and W ions, *Mater. Charact.* **99**, 68 (2015).
- [18] M. A. Tschopp, K. Solanki, F. Gao, X. Sun, M. A. Khaleel, and M. Horstemeyer, Probing grain boundary sink strength at the nanoscale: Energetics and length scales of vacancy and interstitial absorption by grain boundaries in α -Fe, *Phys. Rev. B* **85**, 064108 (2012).
- [19] C. Sun, M. Song, K. Yu, Y. Chen, M. Kirk, M. Li, H. Wang, and X. Zhang, In situ evidence of defect cluster absorption by grain boundaries in Kr ion irradiated nanocrystalline Ni, *Mater. Trans. A* **44**, 1966 (2013).
- [20] X.-M. Bai, L. J. Vernon, R. G. Hoagland, A. F. Voter, M. Nastasi, and B. P. Uberuaga, Role of atomic structure on grain boundary-defect interactions in Cu, *Phys. Rev. B* **85**, 214103 (2012).
- [21] W. Han, M. J. Demkowicz, N. A. Mara, E. Fu, S. Sinha, A. D. Rollett, Y. Wang, J. S. Carpenter, I. J. Beyerlein, and A. Misra, Design of radiation tolerant materials via interface engineering, *Adv. Mater.* **25**, 6975 (2013).

- [22] K. Yu, Y. Liu, C. Sun, H. Wang, L. Shao, E. Fu, and X. Zhang, Radiation damage in helium ion irradiated nanocrystalline Fe, *J. Nucl. Mater.* **425**, 140 (2012).
- [23] S. Wurster and R. Pippin, Nanostructured metals under irradiation, *Scr. Mater.* **60**, 1083 (2009).
- [24] N. Nita, R. Schaeublin, and M. Victoria, Impact of irradiation on the microstructure of nanocrystalline materials, *J. Nucl. Mater.* **329**, 953 (2004).
- [25] Y. Chimi, A. Awase, N. Ishikawa, M. Kobiyama, T. Inami, and S. Okuda, Accumulation and recovery of defects in ion-irradiated nanocrystalline gold, *J. Nucl. Mater.* **297**, 355 (2001).
- [26] M. Rose, A. G. Balogh, and H. Hahn, Instability of irradiation induced defects in nanostructured materials, *Nucl. Instrum. Methods Phys. Res., Sect. B* **127**, 119 (1997).
- [27] T. D. Shen, S. Feng, M. Tang, J. A. Valdez, Y. Wang, and K. E. Sickafus, Enhanced radiation tolerance in nanocrystalline $MgGa_2O_4$, *Appl. Phys. Lett.* **90**, 263115 (2007).
- [28] M. Samaras, P. Derlet, H. Van Swygenhoven, and M. Victoria, Atomic scale modelling of the primary damage state of irradiated fcc and bcc nanocrystalline metals, *J. Nucl. Mater.* **351**, 47 (2006).
- [29] Y. Chen, J. Li, K. Yu, H. Wang, M. Kirk, M. Li, and X. Zhang, In situ studies on radiation tolerance of nanotwinned Cu, *Acta Mater.* **111**, 148 (2016).
- [30] F. Sefta, K. D. Hammond, N. Juslin, and B. D. Wirth, Tungsten surface evolution by helium bubble nucleation, growth and rupture, *Nucl. Fusion* **53**, 073015 (2013).
- [31] G. Odette and D. Hoelzer, Irradiation-tolerant nanostructured ferritic alloys: Transforming helium from a liability to an asset, *JOM* **62**, 84 (2010).
- [32] O. El-Atwani, K. Hattar, J. Hinks, G. Greaves, S. Harilal, and A. Hassanein, Helium bubble formation in ultrafine and nanocrystalline tungsten under different extreme conditions, *J. Nucl. Mater.* **458**, 216 (2015).
- [33] Y. Chen, N. Li, D. Bufford, J. Li, K. Hattar, H. Wang, and X. Zhang, In situ study of heavy ion irradiation response of immiscible Cu/Fe multilayers, *J. Nucl. Mater.* **475**, 274 (2016).
- [34] X.-M. Bai, A. F. Voter, R. G. Hoagland, M. Nastasi, and B. P. Uberuaga, Efficient annealing of radiation damage near grain boundaries via interstitial emission, *Science* **327**, 1631 (2010).
- [35] B. P. Uberuaga, L. J. Vernon, E. Martinez, and A. F. Voter, The relationship between grain boundary structure, defect mobility, and grain boundary sink efficiency, *Sci. Rep.* **5**, 9095 (2015).
- [36] O. El-Atwani, J. Nathaniel, A. Leff, B. Muntifering, J. Baldwin, K. Hattar, and M. Taheri, The role of grain size in He bubble formation: Implications for swelling resistance, *J. Nucl. Mater.* **484**, 236 (2017).
- [37] O. El-Atwani, J. Hinks, G. Greaves, J. Allain, and S. Maloy, Grain size threshold for enhanced irradiation resistance in nanocrystalline and ultrafine tungsten, *Mater. Res. Lett.* **5**, 343 (2017).
- [38] O. El-Atwani, S. Gonderman, M. Efe, G. De Temmerman, T. Morgan, K. Bystrov, D. Klenosky, T. Qiu, and J. Allain, Ultrafine tungsten as a plasma-facing component in fusion devices: effect of high flux, high fluence low energy helium irradiation, *Nucl. Fusion* **54**, 083013 (2014).
- [39] A. Kilmametov, D. Gunderov, R. Valiev, A. G. Balogh, and H. Hahn, Enhanced ion irradiation resistance of bulk nanocrystalline TiNi alloy, *Scr. Mater.* **59**, 1027 (2008).
- [40] O. El-Atwani, J. Nathaniel, A. Leff, K. Hattar, and M. Taheri, Direct observation of sink-dependent defect evolution in nanocrystalline iron under irradiation, *Sci. Rep.* **7**, 1836 (2017).
- [41] A. P. Sutton, R. W. Balluffi, H. Lüth, and J. M. Gibson, Interfaces in crystalline materials and surfaces and interfaces of solid materials, *Phys. Today* **49(9)**, 88 (1996).
- [42] C. M. Barr, G. A. Vetterick, K. A. Unocic, K. Hattar, X.-M. Bai, and M. L. Taheri, Anisotropic radiation-induced segregation in 316L austenitic stainless steel with grain boundary character, *Acta Mater.* **67**, 145 (2014).
- [43] I. Beyerlein, M. Demkowicz, A. Misra, and B. Uberuaga, Defect-interface interactions, *Prog. Mater. Sci.* **74**, 125 (2015).
- [44] S. Zinkle, Microstructure of ion irradiated ceramic insulators, *Nucl. Instrum. Methods Phys. Res., Sect. B* **91**, 234 (1994).
- [45] O. El-Atwani, J. Nathaniel II, A. Leff, J. Baldwin, K. Hattar, and M. Taheri, Evidence of a temperature transition for denuded zone formation in nanocrystalline Fe under He irradiation, *Mater. Res. Lett.* **5**, 195 (2016).
- [46] M. Efe, O. El-Atwani, Y. Guo, and D. R. Klenosky, Microstructure refinement of tungsten by surface deformation for irradiation damage resistance, *Scr. Mater.* **70**, 31 (2014).
- [47] O. El-Atwani, E. Esquivel, M. Efe, E. Aydogan, Y. Wang, E. Martinez, and S. Maloy, Loop and void damage during heavy ion irradiation on nanocrystalline and coarse grained tungsten: Microstructure, effect of dpa rate, temperature, and grain size, *Acta Mater.* **149**, 206 (2018).
- [48] J. F. Ziegler, M. D. Ziegler, and J. P. Biersack, SRIM—the stopping and range of ions in matter (2010), *Nucl. Instrum. Methods Phys. Res., Sect. B* **268**, 1818 (2010).
- [49] J. A. Hinks, J. A. Van Den Berg, and S. E. Donnelly, MIAMI: Microscope and ion accelerator for materials investigations, *J. Vac. Sci. Technol., A* **29**, 021003 (2011).
- [50] P. Jung, *Atomic Defects in Metals (Landolt-Börnstein New Series III/25)*, edited by H. Ullmaier (Springer, Berlin, 1991).
- [51] See Supplemental Material at <http://link.aps.org/supplemental/10.1103/PhysRevMaterials.2.113604> for irradiation damage and ion distribution profiles.
- [52] C. A. Schneider, W. S. Rasband, and K. W. Eliceiri, NIH IMAGE to IMAGEJ: 25 years of image analysis, *Nat. Methods* **9**, 671 (2012).
- [53] E. Elcock, Vacancy diffusion in ordered alloys, *Proc Phys. Soc.* **73**, 250 (1959).
- [54] E. W. Elcock and C. W. McCombie, Vacancy diffusion in binary ordered alloys, *Phys. Rev.* **109**, 605 (1958).
- [55] A. B. Bortz, M. H. Kalos, and J. L. Lebowitz, A new algorithm for Monte Carlo simulation of Ising spin systems, *J. Comput. Phys.* **17**, 10 (1975).
- [56] C. S. Becquart and B. D. Wirth, *Kinetic Monte Carlo Simulations of Irradiation Effects, Comprehensive Nuclear Materials* (Elsevier, London, 2012), p. 3560.
- [57] G. H. Vineyard, Frequency factors and isotope effects in solid state rate processes, *J. Phys. Chem. Solids* **3**, 121 (1957).
- [58] A. Vattré, T. Jourdan, H. Ding, M.-C. Marinica, and M. Demkowicz, Non-random walk diffusion enhances the sink strength of semicoherent interfaces, *Nat. Commun.* **7**, 10424 (2016).
- [59] A. P. Sutton and R. W. Balluffi, *Interfaces in Crystalline Materials* (Clarendon Press, Oxford, 1995).

- [60] F. Dausinger and H. Schultz, Long-Range Migration of Self-Interstitial Atoms in Tungsten, *Phys. Rev. Lett.* **35**, 1773 (1975).
- [61] R. W. Balluffi, Vacancy defect mobilities and binding energies obtained from annealing studies, *J. Nucl. Mater.* **69**, 240 (1978).
- [62] A. Debelle, M. Barthe, and T. Sauvage, First temperature stage evolution of irradiation-induced defects in tungsten studied by positron annihilation spectroscopy, *J. Nucl. Mater.* **376**, 216 (2008).
- [63] M. Griffiths, M. Loretto, and R. Smallman, Electron damage in zirconium: I. Defect structure and loop character, *J. Nucl. Mater.* **115**, 313 (1983).
- [64] M. Gilbert, S. Dudarev, P. Derlet, and D. Pettifor, Structure and metastability of mesoscopic vacancy and interstitial loop defects in iron and tungsten, *J. Phys.: Condens. Matter* **20**, 345214 (2008).
- [65] X. Yi, M. L. Jenkins, M. A. Kirk, Z. Zhou, and S. G. Roberts, In-situ TEM studies of 150 keV W⁺ ion irradiated W and W-alloys: Damage production and microstructural evolution, *Acta Mater.* **112**, 105 (2016).
- [66] Z. Zhang, K. Yabuuchi, and A. Kimura, Defect distribution in ion-irradiated pure tungsten at different temperatures, *J. Nucl. Mater.* **480**, 207 (2016).
- [67] D. Reed, A review of recent theoretical developments in the understanding of the migration of helium in metals and its interaction with lattice defects, *Radiat. Eff.* **31**, 129 (1977).
- [68] M. Demkowicz, R. Hoagland, B. Uberuaga, and A. Misra, Influence of interface sink strength on the reduction of radiation-induced defect concentrations and fluxes in materials with large interface area per unit volume, *Phys. Rev. B* **84**, 104102 (2011).
- [69] N. Juslin, V. Jansson, and K. Nordlund, Simulation of cascades in tungsten–helium, *Philos. Mag.* **90**, 3581 (2010).
- [70] C. Becquart and B. D. Wirth, Kinetic Monte Carlo simulations of irradiation effects, in *Comprehensive Nuclear Materials*, edited by R. J. M. Konings (Elsevier, Amsterdam, 2012), Vol. 1.
- [71] T. Frolov, D. L. Olmsted, M. Asta, and Y. Mishin, Structural phase transformations in metallic grain boundaries, *Nat. Commun.* **4**, 1899 (2013).
- [72] W. Yu and M. Demkowicz, Non-coherent Cu grain boundaries driven by continuous vacancy loading, *J. Mater. Sci.* **50**, 4047 (2015).
- [73] W. Setyawan, G. Nandipati, K. J. Roche, H. L. Heinisch, B. D. Wirth, and R. J. Kurtz, Displacement cascades and defects annealing in tungsten, Part I: Defect database from molecular dynamics simulations, *J. Nucl. Mater.* **462**, 329 (2015).
- [74] X. Yi, M. L. Jenkins, K. Hattar, P. D. Edmondson, and S. G. Roberts, Characterisation of radiation damage in W and W-based alloys from 2 MeV self-ion near-bulk implantations, *Acta Mater.* **92**, 163 (2015).
- [75] G. A. Vetterick, Radiation damage in nanocrystalline iron, Ph.D. thesis, Drexel University, 2014.